Effects of calcination and sintering temperatures on structural profile parameters of modified BNKT-ceramics

Ram Prasad Aryal[*]**, Binod Kumar Bhattarai, Bhadra Pd. Pokhrel**

Department of Applied Sciences and Chemical Eng., Pulchwok campus, T.U, Pulchwok, Lalitpur, Nepal.

[*]*Corresponding author. Email:* aryalram@ioe.edu.np

Abstract

We have carried out a detailed study of synthesis and variations of structural profile parameters: lattice constants, unit cell volume, densities, porosity, crystallite size, dislocation density, and micro-strain of BMZ modified BNKT $(1-x)Bi_{0.5}(Na_{0.70}K_{0.30})_{0.5}TiO_3$-$xBiMg_{0.5}Zr_{0.5}O_3$ for $x = 0, 0.03, 0.06, 0.09$ and 0.12 using X-ray diffraction. The conventional solid-state reaction method was used to synthesize BNKT samples. The BNKT powders were calcined at an optimized temperature of $850°$ C for 2 hours. Keeping the calcination temperature fixed, optimized sintering temperature and time were also determined to be $1140°$ C for 2 hours, based on the sharpness of the peaks and densification. The nature of the XRD patterns is qualitatively similar to that observed for calcined powders; however, the reflections are sharper in sintered samples presumably due to an increase in particle size. The XRD profile reveals an almost pure perovskite structure with cubic symmetries for all samples in both calcined powders as well as sintered samples. The crystallite size, dislocation densities, and micro-strain were determined by using William-Hall plots as well as the Scherrer formula. It is observed that the maximum bulk density was found to be $5.88\,\mathrm{gm/cm^3}$ for $x = 0.03$ which is 96.39% of the theoretical density. The crystallite size varies from $19.84\,\mathrm{nm}$ to $44.15\,\mathrm{nm}$ with compositions for calcined powders and from $57.01\,\mathrm{nm}$ to $62.69\,\mathrm{nm}$ for sintered samples. The very low value of crystallite sizes of calcined powder indicates that the particle size is comparably very low compared to that of sintered samples. The dislocation densities and micro-strain for calcined and sintered powders were observed in the range $(5.1 - 25.4) \times 10^{-4}\,\mathrm{nm^{-2}}$, and $(2.54 - 3.1) \times 10^{-4}\,\mathrm{nm^{-2}}$ and $(1.3 - 4.8) \times 10^{-3}$ and $(8.93 - 9.90) \times 10^{-4}$ respectively which are determined using the William-Hall plot method. These results are also confirmed by the results obtained from the Scherrer method. Both results show improved profile parameters in sintered compositions than in calcination. This verifies that sintered BMZ-doped BNKT powders are promising candidates for many dielectric-based energy storage applications.

1 Introduction

Lead-based ceramics materials such as Lead Zirconium Titanate (PZT) [1] and its derivatives obtained by doping the materials such as Nb, Sn, La, and Ba-modified (PZT) [2–5], Lead Titanate (PT), Lead Magnesium Niobate-Lead Titanate (PMN-PT) [6], etc., have ruled the commercial market of advanced ceramics for more than half a century due to their outstanding superior properties in piezoelectric devices (sensors, actuators, transducers) and in energy harvesting devices (dielectric and supercapacitors). However, during the synthesis process at high temperatures, the volatile nature of Lead caused serious environmental pollution [7] which induced immediate research to develop many lead-free advanced ceramics for various application purposes. So much research work has been done and is ongoing to enhance the properties of conventional eco-friendly ceramics such as $BaTiO_3$ [8], $Bi_{0.5}Na_{0.5}TiO_3$ [9], $K_{0.5}Na_{0.5}NbO_3$ [10], $BiFeO_3$ [11], $SrTiO_3$ [12], $Bi_{0.5}K_{0.5}TiO_3$ [13] that could have efficiency comparable to that of lead-based ceramics [1]. Though there are notable advancements in this area, no lead-free materials could meet the efficiency similar to lead-based materials to serve as a practical substitute for electro-ceramics applications [14–18]. Among the various lead-free ceramics, $Bi_{0.5}(Na\ K)_{0.5}TiO_3$ (BNKT) ceramics have gradually been recognized as one of the best potential candidates for electro-ceramics and have been extensively studied [19, 20]. One of the major problems associated with BNKT ceramics is densification because of the volatile nature of Bi, Na, and K, small sintering temperature range, and potassium sodium ion segregation [10, 21]. Further, in material science, there should be a symbiotic relationship among the five elements i.e. composition-processing-structure-properties-applications for a long time [10]. However, researchers have not paid much attention to the processing parameters as they should be in the BNKT system. So before analyzing the microstructure profiles and their impacts on di-/piezo-/ferroelectric properties, it is important to the optimization of calcination and sintering temperatures in the BNKT ceramics system to obtain high-quality ceramics with enhanced electrical properties.

Polycrystalline solid ceramics are recognized structurally by small segments of high crystallinity. Randomly oriented or textured crystallites are responsible for the formation of anisotropy of the polycrystalline particles. Similarly, the random distribution of atoms in the grain boundaries causes lattice strain and imperfection sources in the lattice that can affect the structural uniformity and overall performance of the material [22, 23]. The analysis of X-ray diffraction peak profiles is a robust technique for characterizing the microstructural attributes of ultrafine-grained materials. Microstructural properties of the material affect their applications. In XRD measurements, photons are dispersed assuming that the crystal is elastic so there is no manifold scattering, no variations in the wavelength, and absorption of energy. According to the kinematical theory, intrinsic factors such as planar defects, dislocations or crystallite size in the microstructure of the material are responsible for the broadening of the diffraction peaks or bands. Examining the distinctive diffraction order dependence makes it possible to distinguish the influences of crystallite size and lattice strain on peak broadening. Standard X-ray diffraction profile analysis procedures, such as assessing the full width at half maximum (FWHM), integral breadths, and Fourier coefficient of the profiles yield information about apparent crystallite size and lattice strain [24–26]. Crystallite size measures the size of coherently diffracting domains. Commonly employed techniques for quantitative analysis include Scherrer's equation, the Williamson-Hall (W-H) method, the Warren-Averbuch analysis, Rietveld refinement, and the pseudo-Voigt function. Nevertheless, the W-H method and Scherrer's equation analyses are widely employed for determining the crystallite size and strain [27].

This paper aims to find an appropriate synthesis temperature and time to have a pure phase of $(1-x)$BNKT-xBMZ ($x = 0.00 - 0.12$) polycrystalline perovskite ceramic material. As reported in the literature, Bi, Na, and K are volatile at high temperatures, so it is important to determine the exact synthesis temperature to get a pure BNKT-based perovskite structure. Next, to carry out a comparative study of the microstructural properties based on the compositions and temperatures. The contribution of crystallite size and microstrain to X-ray diffraction line broadening is analyzed by Scherrer's formula and Williamson–Hall plot methods. The porosities of the resulting samples are also calculated.

2 Materials and Methods

2.1 Materials

Highly pure raw materials of metal oxide-based powders such as Bi_2O_3 (99%), Na_2CO_3 (99.5%), K_2CO_3 (99%), TiO_2 (99%), MgO (99%), and ZrO_2 (99%) all from Sigma–Aldrich were used as starting raw materials.

2.2 Synthesis of (1-x) BNKT-xBMZ powders

Stoichiometrically measured powders were mixed thoroughly for 12 hours at 300 rpm using ethanol and Zirconia balls as ball milling media in a high-energy ball mill (PM400MA, Retsch, Germany). The dried slurry was calcined in the temperature range of 700^0C to 900^0C for 2 hours in a covered crucible. The disk-shaped green pellets were made (approximately 10mm in diameter and 1.2mm in thickness) by mixing 2% PVA as binders into the powders and applying a uniaxial pressure of 10 tons. The green pellets of all the samples were kept at 500^0C for 4 hours to burn off the binder and then sintered in the temperature range of 1090^0C to 1140^0C for 2 hours with a heating rate of 5^0C/min in closed alumina crucibles. During this period, the pellets were embedded with the calcined powders of the same composition to reduce the loss of Bi and Na. The perovskite crystal structure of the sintered powder sample annealed at 500^0C for 8 hours was analyzed by the X-ray diffraction technique using a Powder diffractometer (MiniFlex600, Rigaku, Tokyo, Japan) with CuKα radiation (λ = 1.5406 Å) in the 2θ range from 10^0 to 80^0 with a step size of 0.02^0 and a 2^0/min scanning rate. By using Archimedes' principle, the bulk density of the sintered pellets was measured. The $(1-x)$Bi$_{0.5}$(Na$_{0.7}$K$_{0.3}$)$_{0.5}$TiO$_3$-xBiMg$_{0.5}$Zr$_{0.5}$O$_3$ powder was obtained through ball milling and solid-state reaction by the following equation:

$$(1 - x)[0.25\text{Bi}_2\text{O}_3 + 0.175\text{Na}_2\text{CO}_3 + 0.075\text{K}_2\text{CO}_3 + \text{TiO}_2] + \frac{x}{2}[\text{Bi}_2\text{O}_3 + \text{MgO} + \text{ZrO}_2] \rightarrow (1 - x)\text{Bi}_{0.5}$$
$$(\text{Na}_{0.7}\text{K}_{0.3})_{0.5}\text{TiO}_3 - x\text{BiMg}_{0.5}\text{Zr}_{0.5}\text{O}_3 + 0.25\text{CO}_2$$

(1)
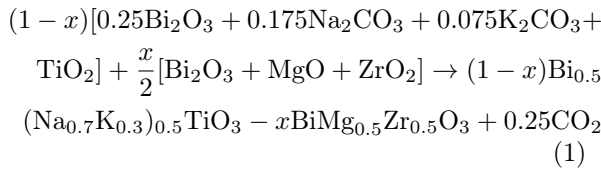
3 Results and Discussion

In this section, we have presented the results and discussion obtained by the X-ray diffraction study. We mainly focused on XRD profile parameters and their analysis.

3.1 Optimization of the operating temperatures

Fig. 1 (a-d) shows the XRD diffraction pattern of the undoped BNKT samples calcined at various temperatures (700^0C-900^0C) for 2 hrs. to optimize the calcination temperature. Based on peak intensities, phase formation, and impurities phases, the calcination temperature was optimized to 850^0C for 2 hrs. as some sorts of small impurity phases were recorded at 800^0C900^0C, which may be due to the volatile nature of Bi and Na at high temperatures or incomplete phase formation in their high composition. In addition, low-intensity peaks were recorded at 700^0C.

Similarly, green pellets prepared at the optimized calcination temperature were sintered at various temperatures (1090^0C-1160^0C) with a soaking time of 2 hrs. at a heating/cooling rate of 5^0C/min to obtain the optimized sintering temperature. Fig. 2 (a-c) shows the corresponding XRD profile patterns. The sample shows some sort of known impurities (to be explained below) at all measured temperatures. Based on densification [28], which is a crucial parameter of sintered ceramics for further characterization and for high device performance, temperature 1140^0C for 2hrs. is set to be an optimized sintering temperature with bulk density (5.78 gm/cm^3). In this way, the working temperature is set up.
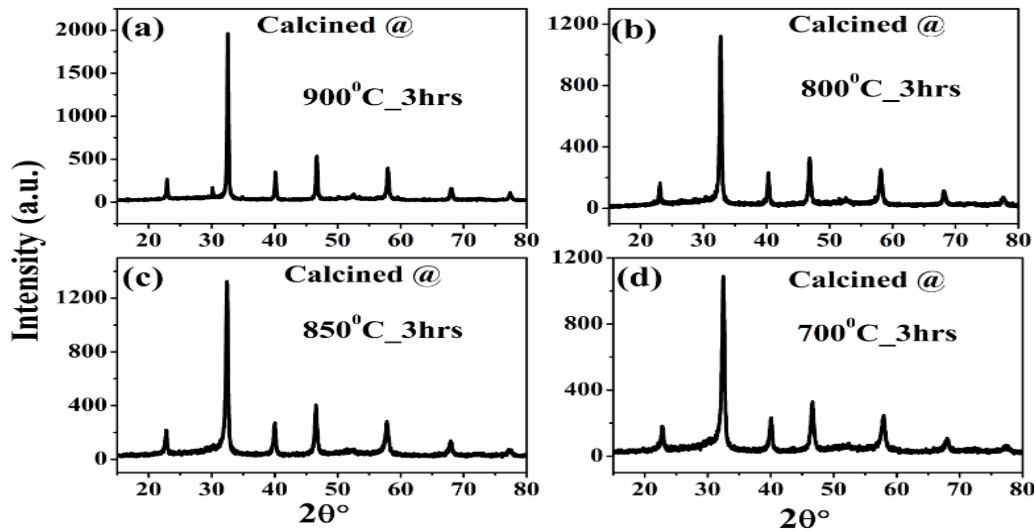

Figure 1: (a-d) XRD patterns of pure BNKT sample calcined at 900^0, 800^0, 850^0 and 700^0C respectively.
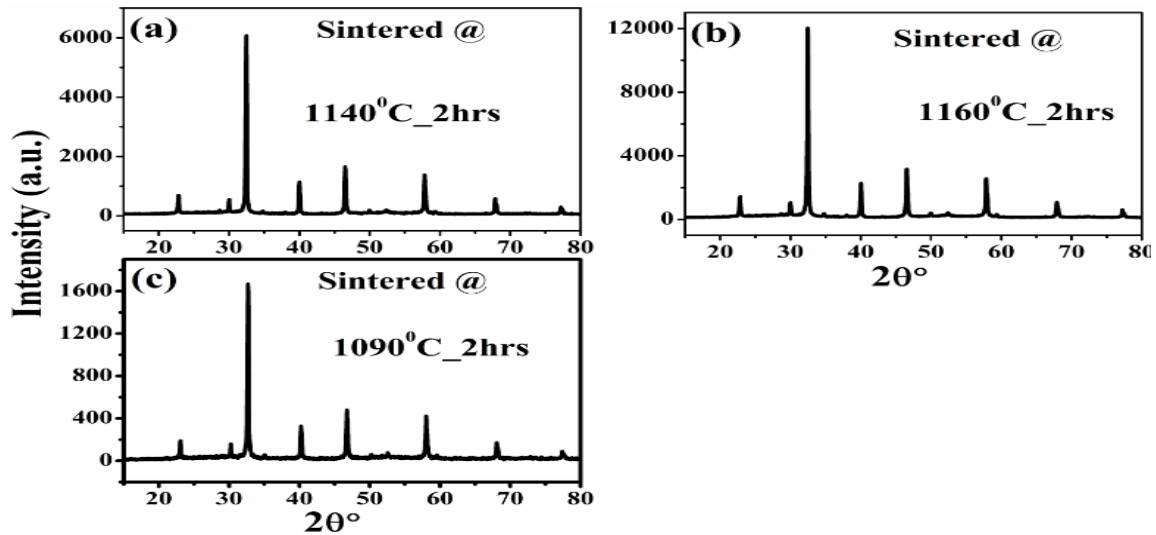
Figure 2: (a-c) XRD patterns of pure BNKT ceramics Sintered at 1140^0, 1160^0, and 1090^0 C..

3.2 Physical, and Structural Analysis

Figures 3 (a, e) and 5 (a, e) show the XRD peak profiles of all calcined and sintered compositions $(x = 0.00 - 0.12)$ separately with enlarged versions of (110) fitted peaks in the inset, respectively. No splitting of (111) and (200) of the peaks recorded for the sintered systems shown in Fig. 7 (a, b) are in good agreement with that of the former reported for other BNT-based ceramics [29, 30], which proposed a structure consisting of cubic phases [31, 32] throughout the entire compositional range.

A small fraction of a known impurity peak called a pyrochlore phase $Bi_2Ti_2O_7$ [28], besides (110) and (200), were seen in some compositions (indicated by ♠) shown in Fig. 5 (a). It has two reasons. First, it is the intermediate phase that can't be transformed into the perovskite structure completely during the nucleation and crystal growth from the amorphous phase. Secondly, because of the volatile nature of Bi and Na at high sintering temperatures, non-stoichiometric structural defects resulted in the formation of a pyrochlore structure [33–37].
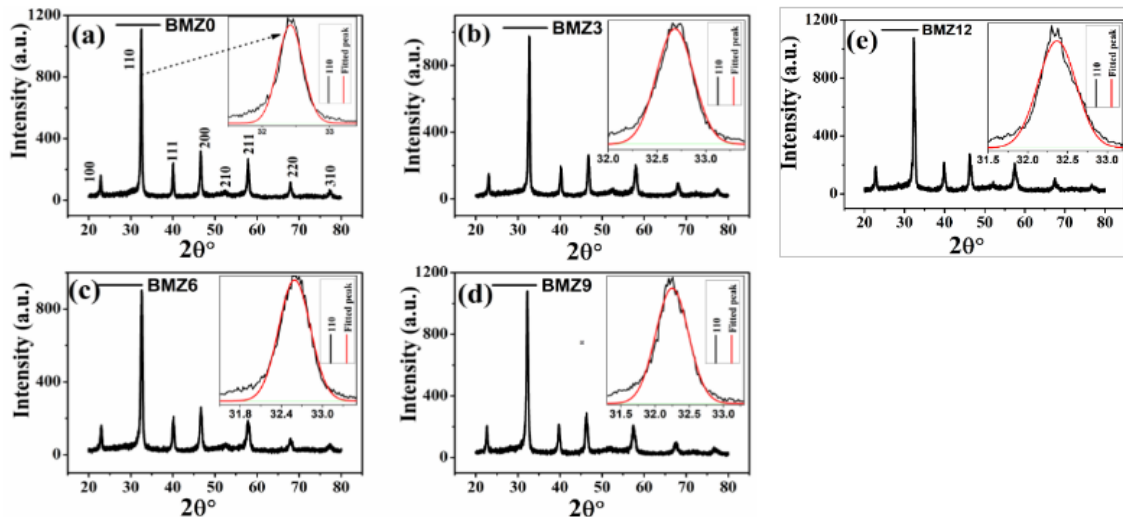

Figure 3: (a-e) XRD patterns of all the calcined samples (x=0.00-0.12) at 850^0C along with enlarged view of (111) peak in the inset image respectively.
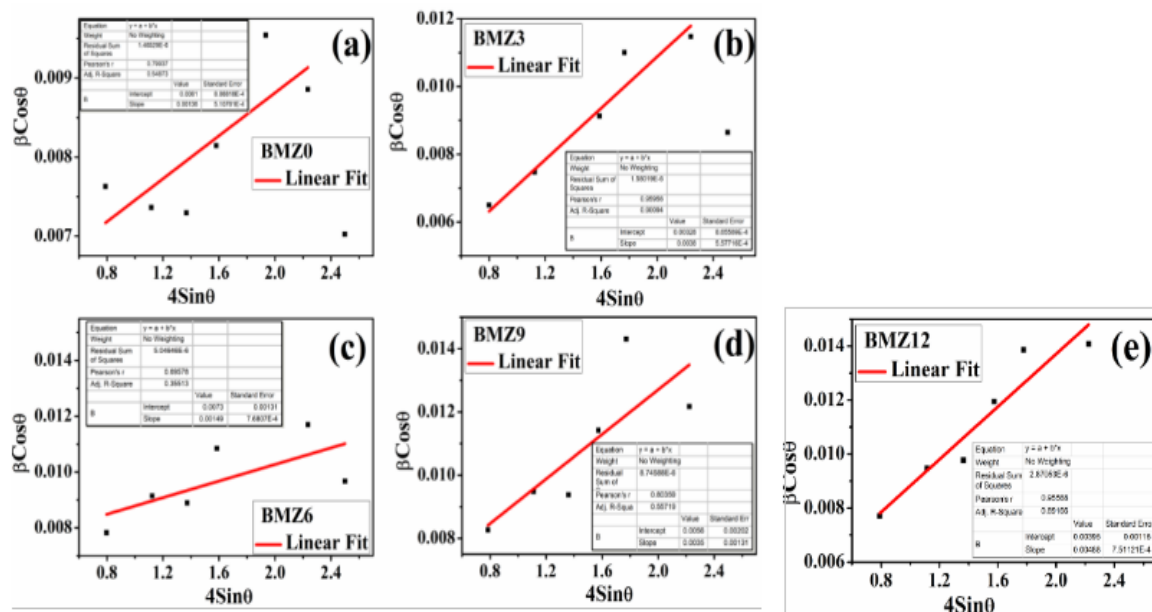
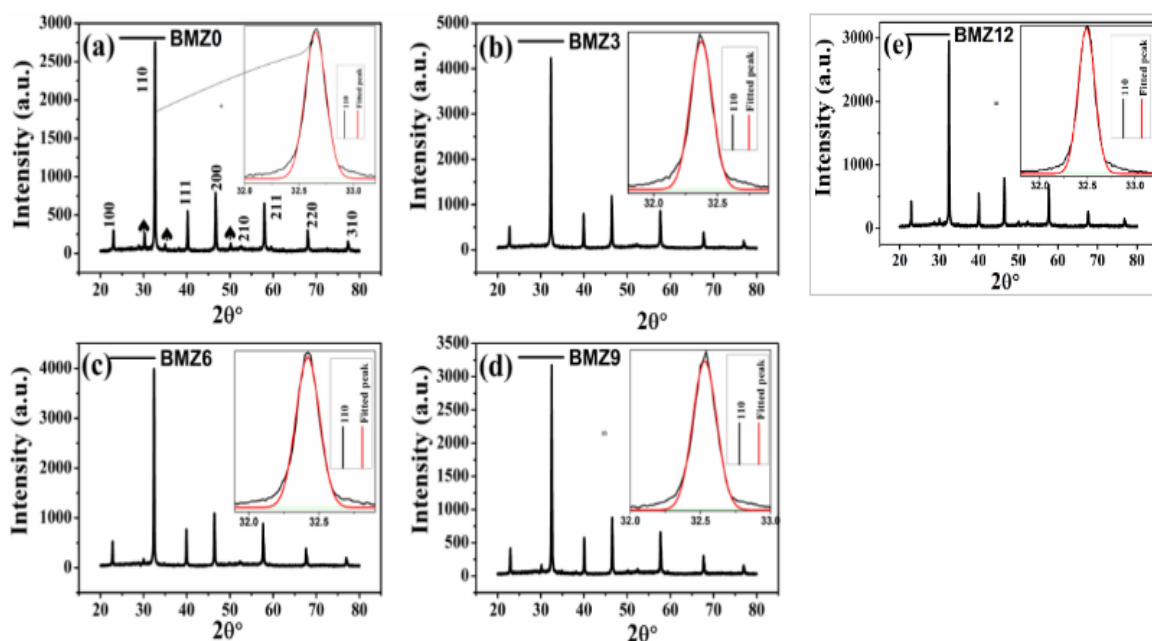Figure 4: (a-e) W-H plots of all the calcined samples (x=0.00-0.12) at 850^0C.

Figure 5: (a-e) XRD patterns of all the Sintered samples (x=0.00-0.12) at 1140^0C along with enlarged view of (111) peak in the inset image respectively.
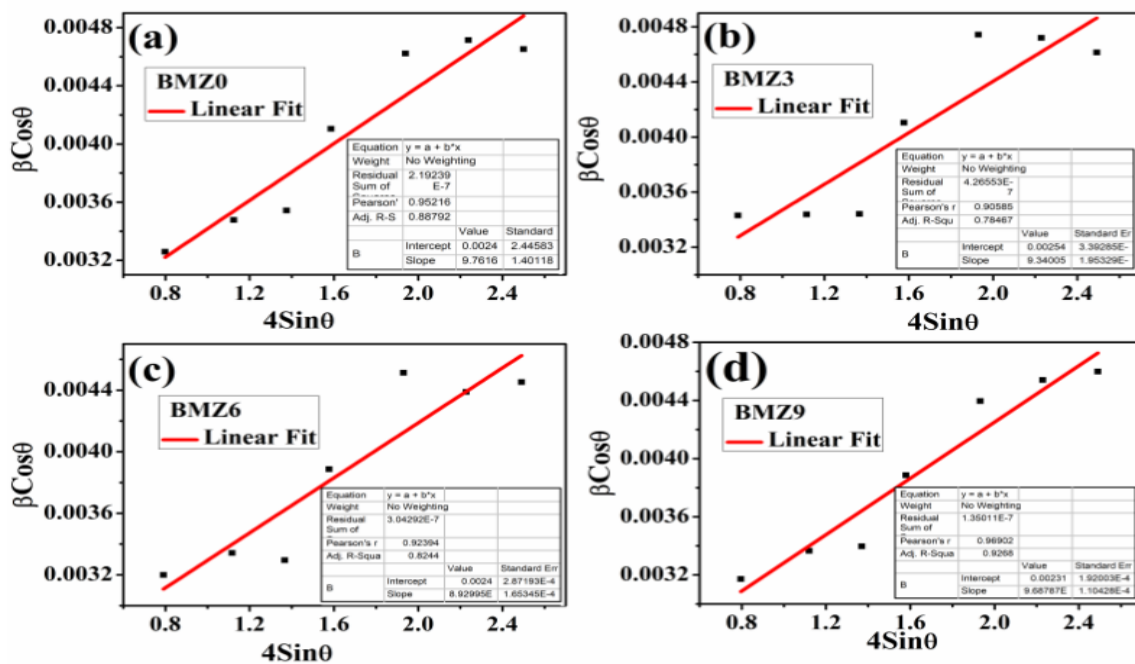
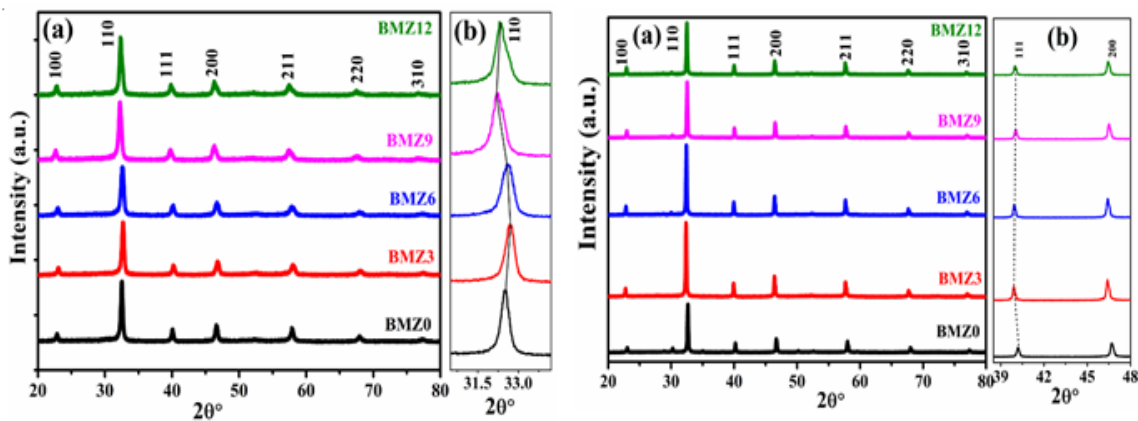Figure 6: (a-e) W-H plots of all the Sintered samples (x=0.00-0.12) at 1140^0C.

Figure 7: (a-b) XRD pattern of all calcined and sintered samples with enlarged peaks (110) of calcined, (111), and (200) for sintered samples respectively.
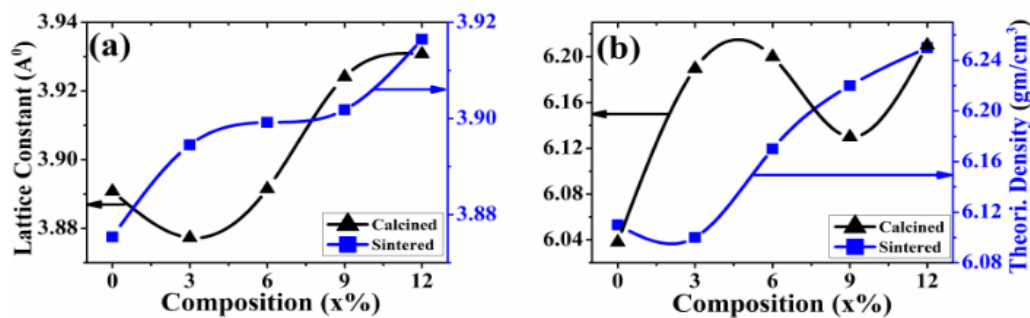

Figure 8: (a-b) Compositional variation of Lattice constant and Theoretical density of calcined and sintered samples respectively.

Table 1: Calculated physical and structural parameters of (1-x) BNKT-xBMZ ceramics at optimized calcination and sintering temperature.

	Calcined Samples			Sintered Samples					
Compositions (x%)	Lattice Constant (Å)	Volume (Å³)	Th. Density (gm/cm³)	Lattice Constant (Å)	Volume (Å³)	Th. Density (gm/cm³)	Bulk Density (gm/cm³)	Rel. Density (%)	Porosity (%)
0	3.8908	58.90	6.04	3.8754	58.20	6.11	5.78	94.5	5.5
3	3.8773	58.29	6.19	3.8945	59.07	6.10	5.88	96.39	3.61
6	3.8915	58.93	6.20	3.8992	59.28	6.17	5.91	95.78	4.22
9	3.9241	60.43	6.13	3.9018	59.58	6.22	5.89	94.69	5.31
12	3.9308	60.74	6.21	3.9165	60.08	6.25	5.83	93.28	6.72

The lattice constant of sintered ceramics gradually increased and reached 3.9165 Å (x=0.12), whereas it decreased at first (x=0.03) and increased in calcined ceramics with BMZ contents, as shown in Fig. 8 (a). The variations of theoretical and relative density (only for sintered ceramics) were plotted and shown in Fig. 8 (b) and Fig. 9 (c), respectively. The maximum relative density of 96.39% was recorded for the sintered composition x=0.03. The porosities of the composition vary from 0.04 - 0.55%. The calculated values of lattice constants, theoretical densities, relative densities, and porosities for all the compositions were also tabulated in Table 1 for a comparative study. The slightly higher value of lattice parameters of calcined parameters than that of sintered samples may be due to the already complete phase formation of all samples.

3.3 Microstructure Analysis

In 1918, Paul Scherrer discovered the first method to compute the crystallite size by employing his equation known as the Scherrer equation [28]. This equation characterizes the broadening of the XRD pattern with crystallite size [38]. The equation is written as

$$\beta cos\theta = \frac{K\lambda}{D} + 4\epsilon sin\theta$$

$$m = \epsilon \text{ (microstrain)}$$

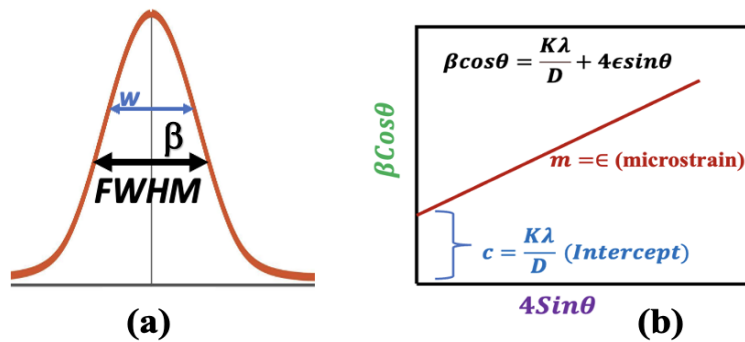$$c = \frac{K\lambda}{D} \text{ (Intercept)}$$

(a) **(b)**

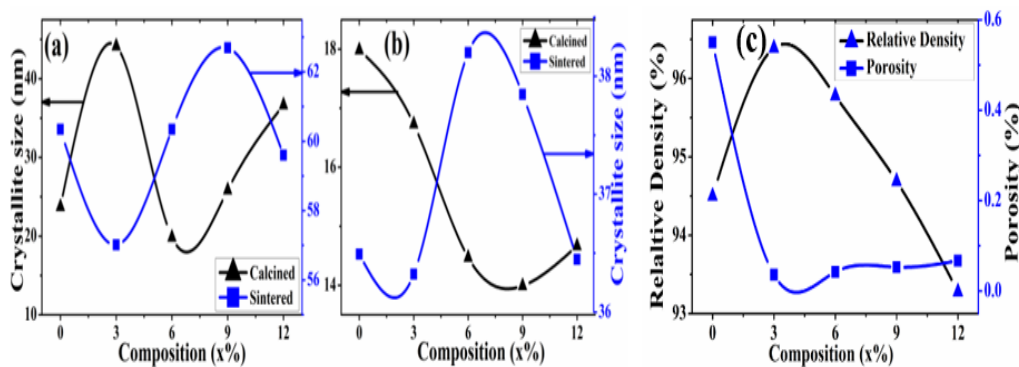Figure 9: FWHM of Broadened X-ray line (b) Schematic plot of Eqn. (6)

Figure 10: (a,b) Compositional variation of Crystallite size of calcined and sintered samples via W-H plot and Scherer's equation method respectively.(c) Compositional variation of Relative density and porosity of sintered samples,
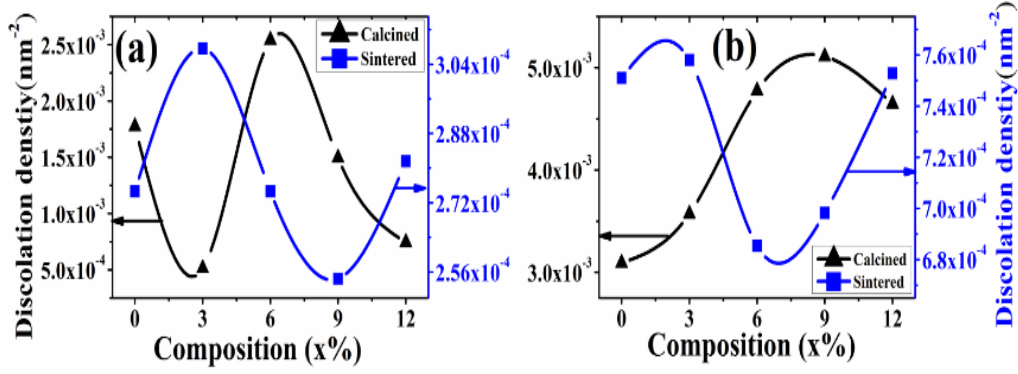
Figure 11: (a, b) Compositional variation of Dislocation density of calcined and sintered samples via W-H plot and Scherer's equation method respectively.
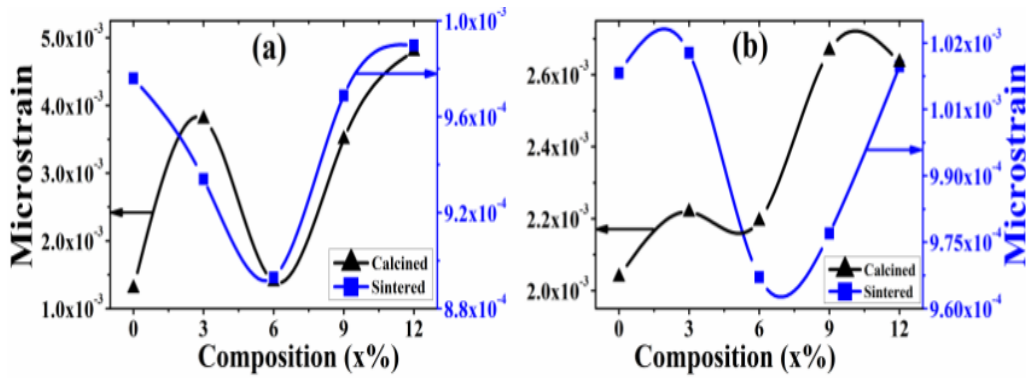

Figure 12: (a, b) Compositional variation of Macrostrain of calcined and sintered samples via W-H plot and Scherer's equation method respectively.

$$\beta = \frac{K\lambda}{D\cos(\theta)} \qquad (2)$$

Where β is the broadening of diffraction peaks (FWHM), K is the Scherrer constant or shape factor (0.94 for FWHM of spherical crystals with cubic symmetry [39]), D is the average crystallite size, θ is Bragg's diffraction angle in degrees, and λ is the X-ray wavelength (CuKα = 1.5405 Å).

Next, the Williamson-Hall (W-H) plot is another method to compute the broadening of X-ray diffraction peaks contributed by crystallite size and lattice strain as they are independent of each other. According to the X-ray line profile analysis, the broadening of the X-ray line results from the microstructure of the material, which is caused by the random distribution of lattice defects within the crystal. The equations involved in the study of peak broadening are [40].

$$\beta = \beta_{\text{crystalline}} + \beta_{\text{strain}} \qquad (3)$$

$$\beta_{\text{crystalline}} = \frac{K\lambda}{D\cos\theta} \qquad (4)$$

$$\beta_{\text{strain}} = 4\epsilon\tan\theta \qquad (5)$$

Using equations (2), (3) and (4) it yields,

$$\beta\cos\theta = \frac{K\lambda}{D} + 4\epsilon\sin\theta \qquad (6)$$

Equation (6) is also termed the expression of the Uniform Deformation Model (UDM) [11]. Where ϵ is the micro-strain. Equation (6) is in the form of $y = mx + c$, where the slope ($m = \epsilon$) measures the micro-strain (ϵ), and the intercept ($c = \frac{K\lambda}{D}$) gives the crystallite size (D) of the W-H plot as shown in Fig. 9 (b).

During the grain growth of the micro/nanoparticles, they experience a lot of compression and relaxation in the lattice, resulting in deviation in the lattice constant as well as an overall deviation in the lattice volume. On the other hand, the displacements of the atoms with respect to the neighboring lattice position result in strain broadening [25]. Micro-strains of all samples are calculated using the following formula based on Scherrer's equation [40].

$$\epsilon = \frac{\beta\cos\theta}{4} \qquad (7)$$

Dislocation is another crucial parameter affecting the nanocrystalline materials' microstructure and performance. It is an imperfection or error in a

crystal associated with one side of the lattice with respect to another part of the lattice within the same crystal. Imperfections in crystals such as dislocations, different vacancies, and interstitials are not uniformly flawed. The dislocation densities (δ) (length of the dislocation lines/volume) are determined by using the X-ray line profile analysis of the samples by using the following relation [40].

$$\delta = \frac{1}{D^2} \qquad (8)$$

Where D is the crystallite size obtained from both Scherrer's equation and W-H plot. The Structural parameters (Crystallite Size, Dislocation density, and Micro-strain) derived from the XRD pattern by using both methods are tabulated in Table 2.

Table 2: Microstructural parameters of calcined and sintered (1-x) BNKT-xBMZ ceramics via Williamson-Hall plot method and Scherrer's Formula method.

Williamson-Hall Plot Method						
Compositions (x%)	Crystallite size (nm)	Dislocation density (nm^{-2})	Microstrain	Crystallite size (nm)	Dislocation density (nm^{-2})	Microstrain
0	23.74	1.77×10^{-3}	1.30×10^{-3}	60.34	2.75×10^{-4}	9.76×10^{-4}
3	44.15	5.13×10^{-4}	3.80×10^{-3}	57.01	3.08×10^{-4}	9.34×10^{-4}
6	19.84	2.54×10^{-3}	1.40×10^{-3}	60.34	2.75×10^{-4}	8.93×10^{-4}
9	25.86	1.50×10^{-3}	3.50×10^{-3}	62.69	2.54×10^{-4}	9.69×10^{-4}
12	36.66	7.44×10^{-4}	4.80×10^{-3}	59.6	2.82×10^{-4}	9.90×10^{-4}
Scherrer's Formula Method						
Compositions (x%)	Crystallite size (nm)	Dislocation density (nm^{-2})	Microstrain	Crystallite size (nm)	Dislocation density (nm^{-2})	Microstrain
0	17.99	3.09×10^{-3}	2.04×10^{-3}	36.49	7.51×10^{-4}	1.01×10^{-3}
3	16.73	3.57×10^{-3}	2.22×10^{-3}	36.32	7.58×10^{-4}	1.02×10^{-3}
6	14.47	4.78×10^{-3}	2.59×10^{-3}	38.2	6.85×10^{-4}	9.67×10^{-4}
9	13.99	5.11×10^{-3}	2.67×10^{-3}	37.84	6.98×10^{-4}	9.77×10^{-4}
12	14.67	4.65×10^{-3}	2.63×10^{-3}	36.45	7.53×10^{-4}	1.01×10^{-3}

The values of crystallite size, microstrain, and dislocation density obtained from W-H Plot and Scherrer's formula methods at two processing temperatures were tabulated in Table 2. Fig. 10 (a, b) shows that crystallite size varies almost in the same manner in both methods but the magnitude of crystallite sizes was quite different between the two methods. Generally, the magnitude of crystallite size calculated from Scherrer's formula for non-zero residual stress is lower than the value obtained from the W-H plot. This is because the assumptions of Scherrer's formula and W-H plot were quite different as mentioned above. It was also seen that the variations of crystallite sizes in calcined and sintered temperatures were in reversed order. The calculated values are in the order of previously reported values in modified BNKT ceramics [41–43]. In comparison, there is a large variation in the average crystallite size obtained from the W-H plot method. This variation occurred as a result of the inequalities in the method of averaging the particle distribution. Based on the data variations in the two methods, Scherrer's formula is more suitable for the determination of crystallite size in this study. Furthermore, the larger the crystallite size, the more crystallinity in the powder. The better crystalline quality corresponds to the lower Urbach energy (an indicator of the electronic quality of thin absorbing materials used in solar cells) [44,45]; so, the sintered sample will show better performance [27].

Figures 11 (a, b) and 12(a, b) show the dislocation density and micro-strain variations computed via both methods, with calcined and sintered temperatures of all compositions. Both parameters were varied in the same manner for both methods. Normally, dislocation in a crystal indicates the defects or imperfections that affect the physical and chemical properties of the crystal. Dislocation densities influence many properties of the materials and it increases with the plastic deformation inside the crystals. Also, it was found that there were compositional variations in the micro-strain values of calcined and sintered samples in both cases. This strain variation could be due to the variations in size and microstructure of the particle [27]. Smaller micro-strain values are seen in sintered composition compared to calcined samples in both cases. On the other hand, by increasing the micro-strain dislocation density increases but grain size decreases, and finally, these parameters reach saturation values [46, 47]. Finally, the result shows the sintered compositions are the best/most applicable sample that holds the best crystalline quality (the least lattice strain, dislocation density, and leads to lower Urbach energy) which enables them to the favorable candidates for optoelectronic devices.

4 Conclusion

The XRD results imply that the (1-x) BNKT-xBMZ bulk ceramic powder was successfully prepared at optimized calcination (850^0 C/2hrs) and sintering (1140^0 C/2hrs) temperatures. Negligible impurity phases were detected in a few compositions. Further, from the literature as well as

peak position and shapes, both calcined and sintered samples are in a cubic phase. Lattice parameters of sintered samples were increased gradually with doping concentration. Micro-structure parameters (crystallite size, dislocation density, and micro-strain) were calculated using the X-ray line profile analysis technique for calcined and sintered samples separately via the W-H plot method and Scherrer's formula. The calculation of most of the crystalline parameters is associated with the corresponding crystallite size and strain. Both methods imply that sintered ceramics' microstructure parameters were better than the calcined samples from the material's application viewpoint. Based on data variations in the two methods, Scherrer's formula fitted well for the determinations of microstructure parameters in this study. X-ray line or diffraction peak analysis is a method, but there still remains more space for future work. For the improvement and precision of the current method, more research and innovation need to be carried out.

Acknowledgesments

References

[1] Y. Hiruma, H. Nagata, and T. Takenaka. Depolarization temperature and piezoelectric properties of $(Bi_{0.5}Na_{0.5})TIO_3$ $(Bi_{0.5}Li_{0.5})TiO_3$–$(Bi_{0.5}K_{0.5})TiO_3$ lead-free piezoelectric ceramics. *Ceram Int*, 35(1):117–120, Jan 2009. 10.1016/j.ceramint.2007.10.023

[2] M. Chandrasekhar and P. Kumar. Synthesis and characterizations of BNT–BT and BNT–BT–KNN ceramics for actuator and energy storage applications. *Ceram Int*, 41(4):5574–5580, May 2015. 10.1016/j.ceramint.2014.12.136

[3] N. Zhang, Y. Feng, and Z. Xu. Effects of lanthanum modification on electrical and dielectric properties of $Pb(Zr_{0.70},Ti_{0.30})O_3$ ceramics. *Mater Lett*, 65(11):1611–1614, Jun 2011. 10.1016/j.matlet.2011.02.087

[4] B. Wang, L. Luo, X. Jiang, W. Li, and H. Chen. Energy-storage properties of (1-x) $Bi_{0.47}Na_{0.47}Ba_{0.06}TIO_3$–xKNbO_3 lead-free ceramics. *J Alloys Compd*, 585:14–18, Feb 2014. 10.1016/j.jallcom.2013.09.052

[5] A. Ullah, C. W. Ahn, A. Hussain, S. Y. Lee, H. J. Lee, and I. W. Kim. Phase transitions and large electric field-induced strain in BiAlO_3-modified $Bi_{0.5}(Na,K)_{0.5}TiO_3$ lead-free piezoelectric ceramics. *Current Applied Physics*, 10(4):1174–1181, Jul 2010. 10.1016/j.cap.2010.02.006

[6] S. Jiang et al. Effect of zr:sn ratio in the lead lanthanum zirconate stannate titanate antiferroelectric ceramics on energy storage properties. *Ceram Int*, 39(5):5571–5575, Jul 2013. 10.1016/j.ceramint.2012.12.071

[7] Z. Yu, Y. Liu, M. Shen, H. Qian, F. Li, and Y. Lyu. Enhanced energy storage properties of bialo3 modified $Bi_{0.5}Na_{0.5}TiO_3$–$Bi_{0.5}K_{0.5}TiO_3$ lead-free antiferroelectric ceramics. *Ceram Int*, 43(10):7653–7659, Jul 2017. 10.1016/j.ceramint.2017.03.062

[8] S. Marković, M. Miljković, Č. Jovalekić, S. Mentus, and D. Uskoković. Densification, microstructure, and electrical properties of batio 3 (bt) ceramics prepared from ultrasonically de-agglomerated bt powders. *Materials and Manufacturing Processes*, 24(10–11):1114–1123, Oct 2009. 10.1080/10426910903031750

[9] Y. Hiruma, H. Nagata, and T. Takenaka. Thermal depoling process and piezoelectric properties of bismuth sodium titanate ceramics. *J Appl Phys*, 105(8), Apr 2009. 10.1063/1.3115409

[10] K. Verma, S. Goel, and R. Sharma. Influence of calcination and sintering temperature on the microstructure, dielectric, ferroelectric and piezoelectric properties of the lead-free knn ceramics. *Journal of Materials Science: Materials in Electronics*, 33(35):26067–26085, Dec 2022. 10.1007/s10854-022-09295-2

[11] V. Ramasamy and et al. Influence of process parameters on the optimization of crystalline phase, size and strain of multiferroic bismuth iron tri oxide (bifeo3) nanoceramics: A mcdm based topsis approach. *Ceram Int*, 46(2):1457–1471, Feb 2020. 10.1016/j.ceramint.2019.09.111

[12] A. Tkach, P. M. Vilarinho, A. M. R. Senos, and A. L. Kholkin. Effect of nonstoichiometry on the microstructure and dielectric properties of strontium titanate ceramics. *J Eur Ceram Soc*, 25(12):2769–2772, Jan 2005. 10.1016/j.jeurceramsoc.2005.03.137

[13] Y. Hiruma, R. Aoyagi, H. Nagata, and T. Takenaka. Ferroelectric and piezoelectric properties of $Bi_{0.5}(Na,K)_{0.5}TiO_3$ ceramics. *Jpn J Appl Phys*, 44(7R):5040, Jul 2005. 10.1143/JJAP.44.5040

[14] S. O. Leontsev and R. E. Eitel. Progress in engineering high strain lead-free piezoelectric ceramics. *Sci Technol Adv Mater*, 11(4):044302, Feb 2010. 10.1143/JJAP.44.5040

[15] J. Rödel, W. Jo, K. T. P. Seifert, E.-M. Anton, T. Granzow, and D. Damjanovic. Perspective on the development of lead-free piezoceramics. *Journal of the American Ceramic Society*, 92(6):1153–1177, Jun 2009. 10.1088/1468-6996/11/4/044302

[16] W. Krauss, D. Schütz, F. A. Mautner, A. Feteira, and K. Reichmann. Piezoelectric properties and phase transition temperatures of the solid solution of $(1\text{-}x)(Bi_{0.5}Na_{0.5})TiO_3\text{–}xSrTiO_3$. *J Eur Ceram Soc*, 30(8):1827–1832, Jun 2010. 10.1016/j.jeurceramsoc.2010.02.001

[17] M. Saleem and et al. Percolation phenomena of dielectric permittivity of a microwave-sintered batio3–ag nanocomposite for high energy capacitor. *J Alloys Compd*, 822:153525, May 2020. 10.1016/j.jallcom.2019.153525

[18] T. Takenaka, H. Nagata, and Y. Hiruma. Current developments and prospective of lead-free piezoelectric ceramics. *Jpn J Appl Phys*, 47(5):3787–3801, May 2008. 10.1143/JJAP.47.3787

[19] P. Butnoi and et al. Effects of processing parameter on phase transition and electrical properties of lead-free bnkt piezoelectric ceramics. *Ferroelectrics*, 511(1):42–51, Apr 2017. 10.1080/00150193.2017.1333364

[20] P. Butnoi, S. Manotham, and T. Tunkasiri. Effect of sintering temperature on mechanical and electrical properties of lead-free $Bi_{0.5}Na_{0.4}K_{0.1}Ti_{0.98}Zr_{0.02}O_3$ piezoelectric ceramics. *Key Eng Mater*, 798:212–217, Apr 2019. 10.4028/www.scientific.net/KEM.798.212

[21] B. Malič and et al. Sintering of lead-free piezoelectric sodium potassium niobate ceramics. *Materials*, 8(12):8117–8146, Dec 2015. 10.3390/ma8125449

[22] C. N. Tomé. Elastic behavior of polycrystals. In *Encyclopedia of Materials: Science and Technology*, page 2409–2415. Elsevier, 2001. 10.1016/B0-08-043152-6/00427-7

[23] A. C. Murrieta and F. F. Contreras-Torres. Microstructure of polycrystalline solids: A brief review from methods in x-ray line profile analysis. *Mater Today Proc*, 48:96–100, Jan 2022. 10.1016/j.matpr.2020.10.978

[24] G. Ribárik, J. Gubicza, and T. Ungár. Correlation between strength and microstructure of ball-milled al–mg alloys determined by x-ray diffraction. *Materials Science and Engineering: A*, 387–389:343–347, Dec 2004. 10.1016/j.msea.2004.01.089

[25] S. S. Jahil and K. H. Harbbi. Development the fourier analysis method of x-ray diffraction to calculate variables in crystal structure as well as calculation of some lattice parameters. *IOP Conf Ser Mater Sci Eng*, 571(1):012112, Jul 2019. 10.1088/1757-899X/571/1/012112

[26] H. P. Klug and L. E. Alexander. *X-Ray Diffraction Procedures: For Polycrystalline and Amorphous Materials*. Wiley, 2nd edition, 1974.

[27] S. Mustapha and et al. Comparative study of crystallite size using williamson-hall and debye-scherrer plots for zno nanoparticles. *Advances in Natural Sciences: Nanoscience and Nanotechnology*, 10(4):045013, Nov 2019. 10.1088/2043-6254/ab52f7

[28] Ch. K. V. Rajulu, S. Ramesh, T. A. Babu, V. Raghavendra, D. Gangadharudu, and K. S. Rao. Structural and modulus spectroscopy studies of bi0.5(na0.8k0.2)0.5tio3 nano-polycrystalline ceramic. *Journal of the Australian Ceramic Society*, 58(1):83–91, Feb 2022. 10.1007/s41779-021-00666-2

[29] M. Wang and et al. Ultrahigh energy storage density and efficiency in bi0.5 na0.5 tio3-based ceramics via the domain and bandgap engineering. *ACS Appl Mater Interfaces*, 13(43):51218–51229, Nov 2021. 10.1021/acsami.1c14151

[30] N. Sun, Y. Li, Q. Zhang, and X. Hao. Giant energy-storage density and high efficiency achieved in $(Bi_{0.5}Na_{0.5})TiO_3\text{–}Bi(Ni_{0.5}Zr_{0.5})O_3$ thick films with polar nanoregions. *J Mater ChMaterialsScienceRefem C Mater*, 6(40):10693–10703, 2018. 10.1039/C8TC03481H

[31] G. O. Jones, J. Kreisel, and P. A. Thomas. A structural study of the $(Na_{1-x}K_x)_{0.5}Bi_{0.5}TiO_3$ perovskite series as a function of substitution (x) and temperature. *Powder Diffr*, 17(4):301–319, Dec 2002. 10.1154/1.1505047

[32] G. O. Jones and P. A. Thomas. Investigation of the structure and phase transitions in the novel a-site substituted distorted perovskite compound Na0.5Bi$_{0.5}$TiO$_3$. *Acta Crystallogr B*, 58(2):168–178, Apr 2002. 10.1107/S0108768101020845

[33] X. J. Zheng and et al. Structural and electrical properties of (Na$_{0.85}$K$_{0.15}$)$_{0.5}$Bi$_{0.5}$TiO$_3$ thin films deposited on lanio3 and pt bottom electrodes. *Appl Surf Sci*, 256(10):3316–3320, Mar 2010. 10.1016/j.apsusc.2009.12.026

[34] H. Dong, X. J. Zheng, W. Li, Y. Q. Gong, J. F. Peng, and Z. Zhu. The dielectric relaxation behavior of (Na$_{0.82}$K$_{0.18}$)$_{0.5}$Bi$_{0.5}$TiO$_3$ ferroelectric thin film. *J Appl Phys*, 110(12), Dec 2011. 10.1063/1.3665389

[35] X. J. Zheng and et al. Effect of potassium content on electrostrictive properties of Na$_{0.5}$Bi$_{0.5}$TiO$_3$-based relaxor ferroelectric thin films with morphotropic phase boundary. *Thin Solid Films*, 548:118–124, Dec 2013. 10.1016/j.tsf.2013.09.017

[36] R. D. Shannon. Revised effective ionic radii and systematic studies of interatomic distances in halides and chalcogenides. *Acta Crystallographica Section A*, 32(5):751–767, Sep 1976. 10.1107/S0567739476001551

[37] A. Hussain, C. W. Ahn, J. S. Lee, A. Ullah, and I. W. Kim. Large electric-field-induced strain in zr-modified lead-free Bi$_{0.5}$(Na$_{0.78}$K$_{0.22}$)0.5TiO$_3$ piezoelectric ceramics. *Sens Actuators A Phys*, 158(1):84–89, Mar 2010. 10.1016/j.sna.2009.12.027

[38] E. F. Crawley and J. de Luis. Use of piezoelectric actuators as elements of intelligent structures. *AIAA Journal*, 25(10):1373–1385, Oct 1987. 10.2514/3.9792

[39] J. I. Langford and A. J. C. Wilson. Scherrer after sixty years: A survey and some new results in the determination of crystallite size. *J Appl Crystallogr*, 11(2):102–113, Apr 1978. 10.1107/S0021889878012844.

[40] R. Verma and et al. Effect of calcination temperature on structural and morphological properties of bismuth ferrite nanoparticles. *Ceram Int*, 47(3):3680–3691, Feb 2021. 10.1016/j.ceramint.2020.09.220.

[41] R. N. Perumal and V. Athikesavan. Structural and electrical properties of lanthanide-doped Bi$_{0.5}$(Na$_{0.80}$K$_{0.20}$)$_{0.5}$TiO$_3$–SrZrO$_3$ piezoelectric ceramics for energy-storage applications. *Journal of Materials Science: Materials in Electronics*, 31(5):4092–4105, Mar 2020. 10.1007/s10854-020-02956-0

[42] M. A. L. Grace, R. Sambasivam, R. N. Perumal, and V. Athikesavan. Enhanced synthesis, structure, and ferroelectric properties of nb-modified (1-x)[Bi$_{0.5}$(Na$_{0.4}$K$_{0.1}$)(Ti$_{(1-X)}$Nb$_x$)]O$_3$x(Ba$_{0.7}$Sr$_{0.3}$)TiO$_3$ ceramics for energy storage applications. *Journal of the Australian Ceramic Society*, 56(1):157–165, Mar 2020. 10.1007/s41779-019-00441-4

[43] N. D. Co and et al. Effect of crystallization temperature on energy-storage density and efficiency of lead-free Bi$_{0.5}$(Na$_{0.8}$K$_{0.2}$)$_{0.5}$TiO$_3$ thin films prepared by sol–gel method. *Journal of Science: Advanced Materials and Devices*, 4(3):370–375, Sep 2019. 10.1016/j.jsamd.2019.04.008

[44] B. Subedi and et al. Urbach energy and open-circuit voltage deficit for mixed anion–cation perovskite solar cells. *ACS Appl Mater Interfaces*, 14(6):7796–7804, Feb 2022. 10.1007/s10853-006-0900-3

[45] M. Ghasemi Hajiabadi, M. Zamanian, and D. Souri. Williamson-hall analysis in evaluation of lattice strain and the density of lattice dislocation for nanometer scaled ZnSe and ZnSe:Cu particles. *Ceram Int*, 45(11):14084–14089, Aug 2019. 10.1007/s10853-006-0900-3

[46] N. Q. Chinh, J. Gubicza, and T. G. Langdon. Characteristics of face-centered cubic metals processed by equal-channel angular pressing. *J Mater Sci*, 42(5):1594–1605, Mar 2007. 10.1021/acsami.1c19122

[47] D. B. Sirdeshmukh, L. Sirdeshmukh, and K. G. Subhadra. *Micro-and Macro Properties of Solids: Thermal, Mechanical and Dielectric Properties.* Springer, 10th edition, 2006. 10.1016/j.ceramint.2019.04.107